JGR Solid Earth

RESEARCH ARTICLE
10.1029/2018JB016673

A Diagenesis Model for Geomechanical Simulations: Formulation and Implications for Pore Pressure and Development of Geological Structures

J. Obradors-Prats[1], M. Rouainia[1], A. C. Aplin[2], and A. J. L. Crook[3]

[1]School of Civil Engineering and Geosciences, Newcastle University, Newcastle upon Tyne, UK, [2]Department of Earth Sciences, Durham University, Durham, UK, [3]Three Cliffs Geomechanical Analysis, Swansea, UK

Abstract Forward basin modeling is routinely used in many geological applications, with the critical limitation that chemical diagenetic reactions are often neglected or poorly represented. Here, a new, temperature-dependent, kinetic diagenesis model is formulated and implemented within a hydromechanical framework. The model simulates the macroscopic effects of diagenesis on (1) porosity loss, (2) sediment strength, (3) sediment stiffness and compressibility, (4) change in elastic properties, (5) increase in tensile strength due to cementation, and (6) overpressure generation. A brief overview of the main diagenetic reactions relevant to basin modeling is presented and the model calibration procedure is demonstrated using published data for the Kimmeridge Clay Formation. The calibrated model is used to show the implications of diagenesis on prediction of overpressure development and structural deformation. The incorporation of diagenesis in a uniaxial burial model results in an increase in overpressure of up to 9 MPa due to both stress-independent porosity loss and overpressure generated by disequilibrium compaction caused by a reduction in permeability. Finally, a compressional model is used to show that the incorporation of diagenesis within geomechanical models allows the transition from ductile to brittle behavior to be captured due to the increase in strength that results in an overconsolidated stress state. This is illustrated by comparison of the present-day structures predicted by a geomechanical-only model, where a ductile fold forms, and a geomechanical model accounting for diagenesis in which a brittle thrust structure is predicted.

Key Points:
- A novel modeling framework is proposed to investigate the macroscopic effects of diagenesis on porosity loss and geomechanical properties
- The ductile/brittle transition behavior observed in Kimmeridge clay samples is successfully captured by the new model
- The likely impact of diagenesis in overpressure and structural style is demonstrated

Correspondence to:
M. Rouainia,
m.rouainia@ncl.ac.uk

Citation:
Obradors-Prats, J., Rouainia, M., Aplin, A. C., & Crook, A. J. L. (2019). A diagenesis model for geomechanical simulations: Formulation and implications for pore pressure and development of geological structures. *Journal of Geophysical Research: Solid Earth*, *124*. https://doi.org/10.1029/2018JB016673

Received 12 SEP 2018
Accepted 2 APR 2019
Accepted article online 8 APR 2019

1. Introduction

Forward basin modeling is a widely used technique capable of capturing the evolution of sediment properties through basin histories, providing useful insights into present-day distributions of stresses, porosity, permeability, pore pressure, and temperature and identifying likely flow pathways which are useful for economic geological applications (e.g., Allwardt et al., 2009; Bekele et al., 2001; Flemings & Lupa, 2004; Kjeldstad et al., 2003; Neumaier et al., 2014; Schneider et al., 2000).

One subtype of basin model is the forward geomechanical model, which has the advantage of simulating lateral deformation and compaction due to tectonic events (e.g., Albertz & Lingrey, 2012; Albertz & Sanz, 2012; Gao et al., 2018; Nikolinakou et al., 2014; Obradors-Prats et al., 2016, 2017a; Smart et al., 2012; Thornton & Crook, 2014). A key limitation of present models is that they only account for the mechanical aspects of compaction, with diagenetic processes generally neglected. In this paper, we refer to diagenesis as all nonmechanical processes that change mineralogy and texture and lead to sediment lithification in relatively low pressure and temperature regimes (i.e., before metamorphism). Diagenesis is critically important since it results in major changes in (a) sediment porosity and permeability (e.g., Bjørlykke & Høeg, 1997; Keller & Isaacs, 1985; Mallon & Swarbrick, 2002; Tada & Siever, 1989), (b) sediment microfabric, cement volume, and geomechanical properties (e.g., Aplin et al., 2006; Day-Stirrat et al., 2008; Ho et al., 1999; Mallon & Swarbrick, 2002; Nygård et al., 2004a, 2004b; Peltonen et al., 2009; Tada, 1991; Walderhaug, 1996), and (c) pore pressure (e.g., Lahann & Swarbrick, 2011; Osborne & Swarbrick, 1997). It is thus essential to incorporate diagenetic reactions (which we call here nonmechanical compaction) into simulations of basin evolution and fluid flow (e.g., Broichhausen et al., 2005; Schneider et al., 1996; Schneider & Hay, 2001). For example, since stiffness and strength exert a first-order control in structural development and stress evolution (Albertz & Lingrey, 2012; Albertz & Sanz, 2012), the incorporation of such diagenetic effects within forward

geomechanical basin models is of great importance for realistic predictions of both fluid flow and structural development.

Previous work in simulating diagenesis within forward basin models has focused mainly on accounting for porosity (and permeability) decrease to predict the resulting increase in pore pressure (e.g. Bolås et al., 2004; Schneider et al., 1996; Schneider & Hay, 2001). Roberts et al. (2015) incorporated a diagenesis model in forward geomechanical simulations which captured the change in sediment properties during opal-A to opal-CT transformation by accounting for both porosity decrease and strength increase due to diagenesis. Nonetheless, in this model the elastic properties and sediment compressibility were considered to remain unchanged after diagenesis, which does not agree with experimental observations on the Kimmeridge Clay (Nygård et al., 2004a, 2004b) and Opalinus Clay (Favero et al., 2016). In contrast, the model presented in this paper captures the compressibility decrease and stiffness increase due to diagenesis.

In this paper, we first present a brief review of the quantitatively most important diagenetic reactions in order to provide a background on the factors controlling their occurrence, the temperature ranges over which they occur and the overprint that these reactions leave on sediment properties. The range and complexity of these reactions are such that it is currently impossible to incorporate their details into a single model. Here, we take a first step by summarizing the findings of a published geomechanical study of the Kimmeridge Clay Formation and highlighting the key observations that serve as the basis for building our model. We then formulate a new, temperature-dependent, kinetic diagenesis model that enables the simulation of nonmechanical porosity loss and its impact on permeability and pore pressure development. Furthermore, the incorporation of diagenetic effects allows the prediction of changes in sediment geomechanical properties such as the overconsolidation state (change in the preconsolidation pressure), the stiffness increase and change in elastic properties. We then demonstrate the workflow for the model calibration using the published Kimmeridge Clay data. Finally, we apply the calibrated diagenesis model in geomechanical basin simulations and discuss its implications for overpressure generation and the predicted structural deformation style.

2. Overview of the Main Diagenetic Reactions Relevant to Basin Modeling

During burial diagenesis, a wide range of chemical reactions cause very significant physical and chemical changes in sediments, generally reducing porosity and permeability, increasing strength, and generating pore pressure. The quantitatively most important of these are the transformations of smectite to illite and opal-A to opal-CT, and quartz and carbonate cementation.

2.1. Smectite to Illite

In mudstones between approximately 70 and 100 °C (ca. 1.7 to 3.5 km depending on surface temperature and geothermal gradient), smectite, or mixed layer illite-smectite (I-S), is converted to illite or more illitic I-S, releasing silica which precipitates as quartz (Berger et al., 1999; Day-Stirrat et al., 2010; Eberl & Hower, 1976; Elliott & Matisoff, 1996; Freed & Peacor, 1989; Hower et al., 1976; Kamp, 2008; Peltonen et al., 2009; Thyberg & Jahren, 2011; Velde & Vasseur, 1992). This process is a dissolution-reprecipation reaction which results in a clay mineral fabric which is increasingly aligned normal to maximum compressive stress (Aplin et al., 2006; Colton-Bradley, 1987; Ho et al., 1999; Swarbrick et al., 2002) and which likely stiffens the mudstone framework (Thyberg & Jahren, 2011).

Because it is a dehydration reaction, water released from the transformation can result in an increase in pore pressure, the magnitude of which depends on the relative rates at which water is (a) generated and (b) lost via fluid flow (e.g., Audet, 1995; Osborne & Swarbrick, 1997; Swarbrick et al., 2002). For a fully drained case (all excess pore pressure is dissipated), porosity loss due to the smectite to illite transformation, attributed to pore collapse due to framework weakening during smectite dissolution (Katahara, 2006; Lahann & Swarbrick, 2011), can be as great as 15 porosity units (Lahann, 2002). During framework weakening, if the pore water cannot escape fast enough, some load previously carried by the framework will be transferred to the fluid, increasing pore pressure (Goulty et al., 2016; Lahann, 2002; Lahann & Swarbrick, 2011).

2.2. Opal-A/Opal-CT

The dissolution of the amorphous phase of opal (opal-A) and reprecipitation as microcrystalline opal-CT occurs at burial depths of 0.1 to 1 km and at temperatures between ~25 and 55 °C (Ishii et al., 2011; Spinelli et al., 2007). In opal-rich sediments, the transition can result in a porosity reduction of up to 15–35% in a reaction zone which may be only 10-m thick (Isaacs, 1981; Meadows & Davies, 2009). At the same time,

the geomechanical properties of the sediments change markedly; for example, Ishii et al. (2011) showed an increase in unconfined compressive strength from 10 to 35 MPa, an increase in tensile strength from ~1 to 4.5 MPa and an increase in cohesion from 3 to 10 MPa. These changes result in sediments which are overconsolidated and with relatively high brittleness.

2.3. Quartz Cementation

Quartz cementation is the primary chemical process route by which porosity is lost in sandstones (Taylor et al., 2010; Worden & Morad, 2000). Silica for quartz cement can come from several sources but is most commonly sourced internally within sands, from intergranular pressure dissolution at styolites or at individual grain contacts (Oye et al., 2018; Walderhaug, 1996). The rate-controlling step for quartz cementation of sandstones is most commonly assumed to be the precipitation of silica (Ajdukiewicz & Lander, 2010; Walderhaug, 1994, 1996), although others have suggested that effective stress plays an important role (Osborne & Swarbrick, 1999; Oye et al., 2018). In this scenario, the kinetic barriers which inhibit quartz precipitation are overcome, on geological timescales, at temperatures around 70 to 80 °C (McBride, 1989; Walderhaug, 1994; Worden & Morad, 2000), above which rates of precipitation increase exponentially with temperature (e.g., Walderhaug, 1996). In addition to reductions in porosity and permeability, quartz cementation increases shear strength due to grain locking, resulting in an increased brittleness of the sediments (Bjørlykke & Høeg, 1997).

2.4. Carbonate Cementation

Although carbonate is a locally important cement in sandstones, we focus here on fine-grained carbonates (chalks and "marls"), which are highly susceptible to intergranular pressure dissolution and chemical compaction. Comparison of porosity-depth trends for experimentally compacted carbonate ooze and natural oozes and chalks shows that below 100 to 200 m, the porosities of natural oozes are much lower than experimentally compacted oozes (Hamilton, 1959; Mallon & Swarbrick, 2002; Scholle, 1977), suggesting the importance of nonmechanical compaction. Solution seams and stylolites are common in calcareous sediments, becoming common in pelagic limestones at depths of 700 to 800 m (Hill, 1987; Tada & Siever, 1989). Carbonate resulting from pressure solution precipitates locally, reducing porosity. Within a stiffer framework, compaction at greater depth is driven by chemical processes, with uncertainty about the extent to which reaction kinetics are controlled by temperature and/or effective stress (Mallon & Swarbrick, 2002). Sediment rheology will be altered because of a cement-related increase in peak strength and cohesion, so that particulate flow is no longer a viable deformation mechanism. This process has been suggested to exert a first-order control on the type of deformation structures formed in some active margins (Sample, 1990).

3. Effects of Diagenesis on Mudrock Properties: The Kimmeridge Clay

One of the best documented examples regarding the effects of diagenesis on the geomechanical properties of clays and shales is the Kimmeridge Clay. Nygård et al. (2004a, 2004b, 2006) performed laboratory experiments, including geotechnical tests, on two sample sets of Kimmeridge Clay collected from two different locations. It was assumed that the two sample sets originated from the same parent materials but had different burial histories prior to uplift. These data are an excellent benchmark for identifying the diagenetic overprint on the geomechanical properties of sediments. This section summarizes the most relevant features of the Kimmeridge Clay in order to serve as a basis for the calibration of the diagenesis model that is presented in section 4.2.

Kimmeridge Clay is an organic-rich, Upper Jurassic sediment deposited in a low-energy intrashelf marine environment. The tested samples in Nygård et al. (2004a, 2004b, 2006) were obtained from two outcrop locations within the Wessex Basin, UK. Kimmeridge Clays from those two locations have been subjected to different burial depths during the Mesozoic and uplifted and exposed during Tertiary inversion. The details about the history and structural evolution of the Wessex Basin are beyond the scope of this paper and the reader is referred to Chadwick (1985), Penn et al. (1987), Selley and Stoneley (1987), Stoneley (1982), and Underhill and Stoneley (1998) for more discussion.

The shallow set of samples were obtained from an open pit in the Westbury Quarry in Wiltshire, UK and will be referred as Kimmeridge Westbury Clay (KWC). The maximum burial depth for KWC is estimated to be about 0.5 km prior to uplift. KWC is dark gray, fissile, uncemented, and rich in fossils. It has a porosity of 0.53 and a grain density of 2.65 g/cm^3 (Kvilhaug, 1995; Nygård et al., 2004a, 2004b).

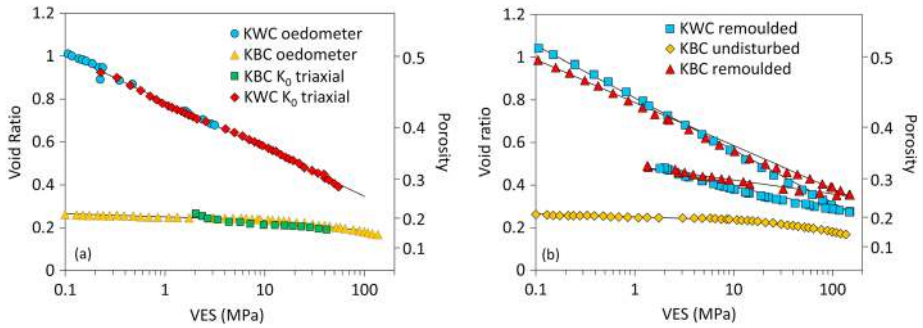

Figure 1. Experimental data for Kimmeridge Westbury Clay (KWC) and Kimmeridge Bay Clay (KBC). The figures were obtained from Nygård et al. (2004a). (a) Compaction curves for undisturbed KWC and KBC samples obtained from an oedometer and a K_0 triaxial test. (b) Compaction and unloading curves for remolded samples of KWC and KBC and compaction curve of an undisturbed sample of KBC.

The deep set of samples were obtained from Kimmeridge Bay, Isle of Purbeck, Dorset, UK, and will be referred to as Kimmeridge Bay Clay (KBC). This area was buried about 1.7–2 km before being uplifted, with a maximum vertical effective stress of about 20 MPa and a maximum temperature around 80 °C. KBC is black, laminated, lithified/cemented, and splits easily along its lamination. The initial porosity for KBC is 0.22, substantially lower than KWC, but its grain density of 2.64 g/cm^3 is similar to that of KWC.

The geotechnical investigation comprises a set of uniaxial strain compaction tests on undisturbed and remolded samples at different water contents for both KWC and KBC performed using oedometer and advanced triaxial apparatus. The tests were carried out up to a maximum vertical effective stress of 120 MPa. The permeability normal to the bedding plane was also measured as a function of porosity. In addition, a set of undrained shear tests were undertaken at different confining pressures on both KWC and KBC. For a complete description of materials and test procedures the reader is referred to the original papers by Nygård et al. (2004a, 2004b, 2006).

Figure 1a shows the compaction curves in a logarithmic vertical effective stress-void ratio plot for undisturbed samples of KWC and KBC. Both samples have very different initial porosities due to their different void ratios at 0.1 MPa. Another trivial observation from the plot is that the compressibility index (decrease in void ratio for a given increase in stress) of the two clay materials is significantly different, with the slopes of the best fitting straight lines being 0.221 and 0.060 for KWC and KBC, respectively. This shows that KBC exhibits a stiffer behavior compared to KWC. This difference has been attributed to the deeper burial and lithification of KBC, which facilitated the formation of a stiffer matrix. It is interesting to note that even at stresses above the maximum that KBC has experienced during its burial history (estimated to be around 20 MPa), the porosity for KWC is about 15 porosity units higher than that for KBC, which would suggest that nonmechanical compaction processes have contributed to the decrease of porosity in KBC. In addition, the unloading/reloading curves on remolded KWC and KBC samples (which correspond to the mechanically overconsolidated compaction curves), shown in Figure 1b, are significantly steeper than the compaction curve of undisturbed KBC. Nonmechanical processes must therefore have contributed to the increased stiffness (reduced compressibility) of KBC. The diagenesis model presented in this work aims to capture and simulate all these reported observations.

4. Modeling Strategy

The diagenesis model presented in this paper has been implemented within the finite element code ParaGeo (Crook, 2013). The code encompasses procedures for both fully implicit and quasistatic explicit simulations for computational viscoplasticity at finite strains and localization. In coupled geomechanical/porous flow problems, the solid phase has a Lagrangian reference frame, whereas the fluid phase has an Eulerian reference frame (i.e., the fluid flows through the mesh of the solid phase). The code models sedimentation by generating new elements to represent the sedimented material and includes robust remeshing procedures for handling pinch-out of stratigraphy and excessive mesh distortion due to large strains. In addition, the framework includes a procedure for energy regularization during softening based on fracture mechanics principles.

4.1. Constitutive Model

The diagenesis model presented in this paper is modular and could be coupled to any modified Cam-clay constitutive model. Here we adopt the so-called Soft Rock 4 (SR4) critical state model, and the most relevant aspects of the critical state constitutive model for this paper will be summarized. For more details on the formulation of SR4 the reader is referred to Obradors-Prats et al. (2016, 2017a, 2017b).

First, we start by considering the decomposition of the effective stress tensor, σ', into deviatoric and volumetric parts (Terzaghi, 1923):

$$\sigma' = \boldsymbol{s} + p'\boldsymbol{I} \quad \text{with} \quad p' = \frac{1}{3}\text{tr}[\boldsymbol{\sigma}'] \tag{1}$$

where p' denotes the effective mean stress, s is the deviatoric stress tensor, I is the second-rank identity tensor, and tr[·] is the trace operator of [·]. In addition to the effective mean stress, the deviatoric stress $q = \sqrt{\frac{2}{3}(\mathbf{s} : \mathbf{s})}$ is needed in the constitutive formulation of the yield surface and flow potential. The deviatoric stress can be written in terms of the three principal effective stresses $\sigma 1'$, $\sigma 2'$, and $\sigma 3'$ as $q = \sqrt{\frac{1}{2}\left[(\sigma'_1 - \sigma'_2)^2 + (\sigma'_1 - \sigma'_3)^2 + (\sigma'_2 - \sigma'_3)^2\right]}$.

It may be noted that for sediments buried under uniaxial strain conditions (i.e., $\sigma'_2 = \sigma'_3$) the definition of deviatoric stress, widely adopted in critical state soil mechanics (e.g., Muir Wood, 1990; Rouainia & Muir Wood, 2006), coincides with the definition of differential stress used in geophysics and structural geology literature ($q = \sigma'_1 - \sigma'_3$).

The yield surface for a sediment as described in critical state soil mechanics bounds the region of elastically accessible stress states in the p'-q plane characterized by elastic strains (stress paths moving inside the yield surface). The critical state line divides the yield surface in two parts; the cap side (compression part) and the shear side. Yielding on the cap side results in shear-enhanced compaction and sediment hardening, which macroscopically results in ductile diffuse plastic strain. On the other hand, yielding on the shear side leads to dilative sediment softening and strain localization. Yielding on the critical state results in continuous shear at both constant effective stress and constant volume. The yield surface is defined with two functions that intersect at the maximum deviatoric stress in the p'-q plane as

$$f(p', \varepsilon_v^p) = \begin{cases} g(\theta, p')q + (p' - p_t)\tan\beta\left[\frac{(p'-p_c)}{(p_t-p_c)}\right]^{1/n}, & \text{if } p' \geq p_{\phi_{\text{peak}}} \\ \left[g(\theta, p')\right]^2 q^2 - M_\phi^2 p_{\phi_{\text{peak}}}^2 \left[1 - \frac{(p_{\phi_{peak}} - p')^2}{(p_{\phi_{peak}} - p_c)^2}\right], & \text{if } p' < p_{\phi_{\text{peak}}} \end{cases} \tag{2}$$

where p' is the mean effective stress, q is the deviatoric stress, p_t is the tensile intercept of the yield surface with the hydrostatic axis, p_c is the preconsolidation pressure or compressive intercept of the yield surface with the hydrostatic axis, $p_{\phi_{\text{peak}}}$ is the effective mean stress at q peak value, ε_v^p is the plastic volumetric strain, M_ϕ is the slope of the line that intersects both the origin of the p'-q space and the yield surface in q peak value, β and n are material constants which define the shape of the yield surface in the p'-q plane, $g(\theta, p')$ is a function that describes the shape of the yield surface in the deviatoric plane (plane normal to the hydrostatic axis), and θ is the Lode's angle, which can be related to $\sigma 1'$, $\sigma 2'$, and $\sigma 3'$ as

$$-\frac{\pi}{6} \leq \theta = \tan^{-1}\left[\frac{1}{\sqrt{3}}\left(\frac{2\sigma'_3 - \sigma'_1 - \sigma'_2}{\sigma'_1 - \sigma'_2}\right)\right] \leq \frac{\pi}{6} \tag{3}$$

The shape of the plastic potential is defined by a function similar to the yield surface but with two different shape parameters causing the flow rule to be nonassociative:

$$\psi(p', \varepsilon_v^p) = \begin{cases} q + (p' - p_t)\tan\psi\left[\frac{(p'-p_c)}{(p_t-p_c)}\right]^{(1/m)} & p' \geq p_{\psi_{\text{peak}}} \\ q^2 - M^2 p_{\psi_{\text{peak}}}^2 \left[1 - \frac{(p_{\psi_{\text{peak}}} - p')^2}{(p_{\psi_{\text{peak}}} - p_c)^2}\right] & p' < p_{\psi_{\text{peak}}} \end{cases} \tag{4}$$

where M is the slope of the critical state line, $p_{\psi_{\text{peak}}}$ is the effective mean stress at q peak value for the flow potential, ψ and m are two material constants, which define the shape of the flow potential surface in p'-q plane. Note that for $n = m$, $p_{\phi_{\text{peak}}}$ coincides with $p_{\psi_{\text{peak}}}$ so that the critical state is located at the peak strength. In contrast to the yield function, the flow potential surface has a circular shape in the deviatoric plane for all values of p_c since it does not depend on the Lode's angle or include any deviatoric correction term.

The hardening law, which describes the evolution of the yield surface as a function of plastic strain, is defined as

$$p_c = p_{c0} \exp\left[-\frac{v\varepsilon_v^p}{(\lambda-\kappa)}\right] \tag{5}$$

and

$$p_t = p_{t0} \exp\left[-\frac{v(\varepsilon_v^p)_{\max}}{(\lambda-\kappa)}\right] \tag{6}$$

where $v = 1 + e$ is the specific volume with e being the void ratio, λ and κ are the slopes of the normal compression line and unloading-reloading line in a v-ln p' compression plane and $(\varepsilon_v^p)_{\max}$ is the maximum dilatational volumetric plastic strain.

The poroelastic strains resulting from stress paths moving inside the yield surface are described by the stress and bulk modulus, K_b defined by a non-linear porosity and stress dependent function as:

$$K_b = K_{b0} + (1 - A_{\text{un}})\frac{p_c}{\kappa} + A_{\text{un}}\frac{p'}{(1-\phi)\kappa} \tag{7}$$

where K_b is the bulk modulus, K_{b0} is the bulk modulus at deposition (i.e., when $p_c \to 0$ and $pm' \to 0$), ϕ is the porosity, and A_{un} is the dependence factor which has values $0 \leq A_{un} \leq 1$.

4.2. Diagenesis Model

Numerous factors control the occurrence and intensity of diagenetic processes, including temperature, mineralogy, fabric, geochemistry of the pore fluids, etc. To simplify the representation of these processes, the diagenesis model adopts a phenomenological approach that captures the first-order macroscopic effects that diagenetic processes have on sediments. The specific components are as follows:

- Reaction model, defining the rate of volume reduction and total potential volume reduction.
- Compaction model, defining the changes of the hardening moduli and preconsolidation pressure.
- Cementation model, for example, defining change in bond strength.
- Flow rule, defining whether the volume change is predominantly uniaxial or hydrostatic.

These processes are dependent on temperature and time and also an assumed maximum porosity change for the model, which is called here *nonmechanical compaction*.

At a given time the current porosity, ϕ, is expressed as

$$\phi = \phi_0 + (\Delta\phi)^{\text{mech}} + (\Delta\phi)^{\text{diag}} \tag{8}$$

where ϕ_0 is the reference or initial porosity, $(\Delta\phi)^{\text{mech}}$ and $(\Delta\phi)^{\text{diag}}$ are the porosity changes due to mechanical and diagenetic processes, respectively. Several chemical reactions taking place at different depths may contribute to the total diagenetic porosity change. Consequently, the total diagenetic porosity change is evaluated as the sum of the diagenetic porosity change for all reactions:

$$\Delta\phi^{\text{diag}} = \sum_{i=1}^{N} (\Delta\phi)_i^{\text{diag}} \tag{9}$$

where $(\Delta\phi)_i^{\text{diag}}$ is the diagenetic porosity change for the ith reaction and N is the total number of chemical reactions. The rate of porosity loss for a given reaction i is then defined by the following power law:

$$\frac{\mathrm{d}\phi_i^{\text{diag}}}{\mathrm{d}t} = -A\left(\frac{T - T_{\text{ini}}}{T_{\text{ini}}}\right)^{m_d}\left[\frac{(\Delta\phi)_{i,\max}^{\text{diag}} - (\Delta\phi)_i^{\text{diag}}}{(\Delta\phi)_{i,\max}^{\text{diag}}}\right]^{n_d} \tag{10}$$

where T is the current temperature, T_{ini} is the threshold temperature above which the reaction begins to occur, m is an exponent for the temperature-dependent term, $(\Delta\phi)_{i,\max}^{\text{diag}}$ is the maximum porosity loss due to the ith chemical reaction, n is an exponent for the porosity change-dependent term and A (1/Ma) is a constant. The diagenetic porosity loss may be either isotropic or orthotropic (e.g., uniaxial in the direction of the maximum compressive stress). This allows us to represent the behavior of specific reactions (e.g., volume loss as a result of pressure solution might be better represented by an orthotropic law).

Table 1
Material Parameters for the SR4 Model for Clay (Syntectonic Sediments) and Shale (Preexisting Sediment Wedge) Lithologies

Modelling feature	Parameter	Symbol	Value
Yield surface p'-q	Preconsolidation pressure at deposition	p_{c0}	0.1 MPa
plane	Tensile intercept at deposition	p_t	−0.01 MPa
	Friction parameter	β	52°
	Yield surface exponent	n	1.6
Yield surface shape	Deviatoric plane exponent	N^{π}	0.25
in the deviatoric plane	Deviatoric plane parameter	β_0^{π}	0.6
	Deviatoric plane parameter	β_1^{π}	0.6
Flow potential surface	Dilation parameter	ψ	45°
	Flow potential exponent	m	1.6
Hardening law and	Poisson ratio	μ	0.3
elasticity	Bulk modulus at deposition	K_0	10 MPa
	Depositional porosity	Φ_0	51.05%
	Hardening modulus	λ	0.11
	Slope of the unloading/reloading line	κ	0.05
	Porosity-dependence factor	A_{un}	0.5
Grain properties	Grain density	ρ_s	2,650 kg/m^3
	Grain stiffness	k_s	20,000 MPa
Fluid properties	Fluid density	ρ_f	1,000 kg/m^3
	Fluid stiffness	k_f	2,000 MPa
	Fluid viscosity	μ_f	3.171×10^{-23} (MPa-Ma)

In addition to the porosity loss, the diagenetic processes induce changes in the rock fabric, mineralogy, and texture due to the dissolution and precipitation of minerals. These changes may in turn affect the geomechanical properties, such as rock strength and compaction behavior. This is accounted for by updating the hardening parameter and the slope of the elastic unloading/reloading line, in the v-ln p' plane, according to the following expressions:

$$\lambda = \lambda^{\mathrm{mech}} + (\Delta\lambda)^{\mathrm{diag}}_{\mathrm{max}} \left[\frac{\Delta\phi^{\mathrm{diag}}}{\Delta\phi^{\mathrm{diag}}_{\mathrm{max}}}\right] \tag{11}$$

$$\kappa = \kappa^{\mathrm{mech}} + (\Delta\kappa)^{\mathrm{diag}}_{\mathrm{max}} \left[\frac{\Delta\phi^{\mathrm{diag}}}{\Delta\phi^{\mathrm{diag}}_{\mathrm{max}}}\right] \tag{12}$$

where λ^{mech} and κ^{mech} are the slopes of the normal compression and unloading-reloading lines in a v-ln p' plane without the diagenesis contribution, respectively, and $(\Delta\lambda)^{\mathrm{diag}}_{\mathrm{max}}$ and $(\Delta\kappa)^{\mathrm{diag}}_{\mathrm{max}}$ are the maximum changes in λ and κ due to diagenesis. The increase in sediment strength (increase in the preconsolidation pressure) due to diagenesis is accounted for by including the diagenetic volumetric plastic strain, $\Delta\varepsilon^{p(\mathrm{diag})}_{v(\mathrm{mech})}$ to the total volumetric strain; that is, the volumetric plastic strain used to compute the preconsolidation pressure in equation (5) is now defined as

$$\Delta\varepsilon_v^{p(\mathrm{hard})} = \Delta\varepsilon_v^{p} + \Delta\varepsilon^{p(\mathrm{diag})}_{v(\mathrm{mech})} \tag{13}$$

where $\Delta\varepsilon_v^{p(\mathrm{hard})}$ is the volumetric plastic strain that is used to evaluate strength, $\Delta\varepsilon_v^{p}$ is the mechanical volumetric plastic strain and

$$\Delta\varepsilon^{p(\mathrm{diag})}_{v(\mathrm{mech})} = \frac{\Delta t}{1-\phi}\sum_{i=1}^{N} F_{\mathrm{pc}_i}\frac{\mathrm{d}\phi_i^{\mathrm{diag}}}{\mathrm{d}t} \tag{14}$$

where Δt is the time increment and F_{pc_i} is a nondimensional scaling parameter which controls the proportion of the diagenetic volumetric plastic strain that contributes toward the increase in strength.

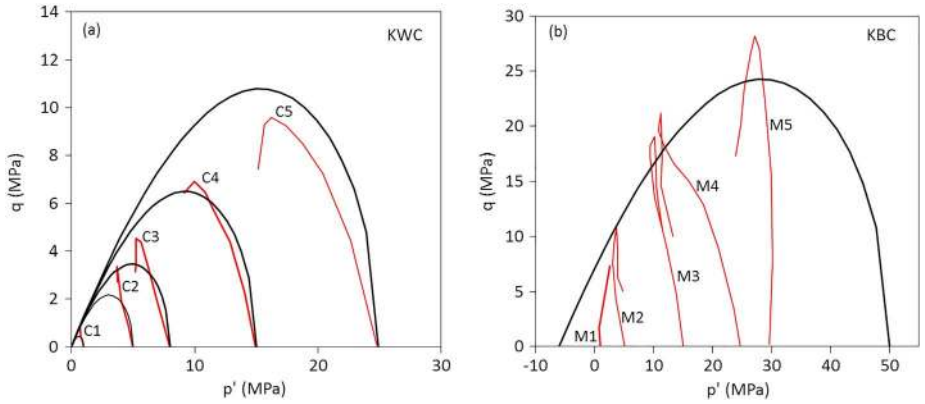

Figure 2. Effective stress paths for undrained shearing of Kimmeridge Westbury Clay (KWC) (a) and Kimmeridge Bay Clay (KBC) (b) samples. The data have been obtained from Nygård et al. (2006) and the C1, C2, … M5 stand for their original labels. The shown yield surfaces are the best fit shape after calibration obtained under the following assumptions: (1) the same yield surface shape parameters should be used for KWC and KBC (the diagenesis has not changed the yield surface shape), (2) KWC samples are all normally consolidated, so the stress paths should approximately follow the cap side of their respective yield surfaces, and (3) KBC samples are all overconsolidated, so the peak stress of the stress paths should be approximately located on the shear side of the common yield surface.

Cementation of minerals within the pore spaces of sediments creates bonds between particles. Macroscopically, the effect of cementation is an increase of the tensile intercept of the yield surface with the hydrostatic axis, that is,

$$p_t = p_t^{\text{mech}} + (\Delta p_t)_{\text{max}}^{\text{diag}} \left[\frac{\Delta \phi^{\text{diag}}}{\Delta \phi_{\text{max}}^{\text{diag}}} \right] \tag{15}$$

where p_t^{mech} is the tensile intercept without the contribution of diagenesis and $(\Delta p_t)_{\text{max}}^{\text{diag}}$ is the maximum increase in the tensile intercept due to diagenesis. Note that the increase in the tensile intercept due to cementation may be reversed due to mechanically induced destructuration and bond breakage.

5. Model Calibration

The new constitutive model has been specifically calibrated to reproduce the experimental results of samples from KWC and KBC to ensure that the diagenesis model is able to capture the transition from KWC to KBC mechanical properties. This procedure is performed in two steps: first, a mechanical compaction-only model is calibrated for the KWC and second, a diagenesis reaction is calibrated for a model that can simulate the whole Kimmeridge Clay history, starting with KWC mechanical properties and simulating its transition to KBC. The set of material parameters, which has been used for matching all the KWC data is shown in Table 1.

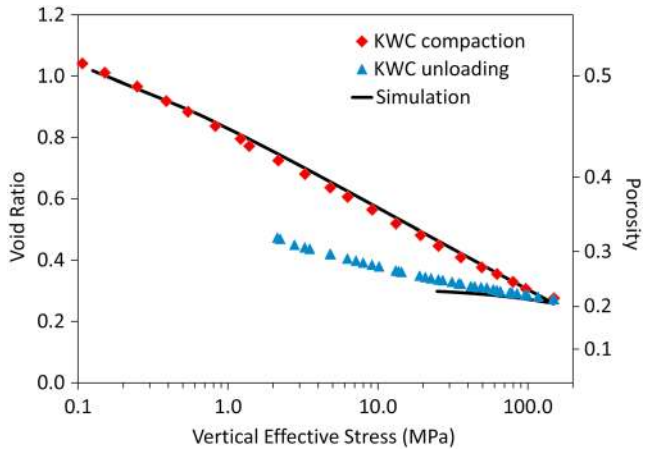

Figure 3. Results of an oedometer test model for Kimmeridge Westbury Clay (KWC) after material calibration. The data for compaction and unloading have been obtained from Nygård et al. (2004a).

The shape of the yield surface for KWC and KBC is assumed to be the same (i.e., the change of yield surface due to nonmechanical compaction is via expansion due to diagenetic-induced strengthening). Consequently, the yield surface is calibrated to provide a best fit to individual undrained shear stress paths of KWC and KBC (Nygård et al., 2006). It has been assumed that all KWC samples were in a normally consolidated state. Consequently, the yield surface for each test increases in size during the isotropic consolidation stage prior to the shearing stage. Subsequently, the stress paths have followed approximately the cap side of the yield surface in each test until they reached the peak stress (see Figure 2a). In addition, it has been assumed that all the KBC samples were overconsolidated. As a result, we assume that the peak stress reached during the shear test in all the samples is approximately located on the shear side of a common yield surface (see Figure 2b).

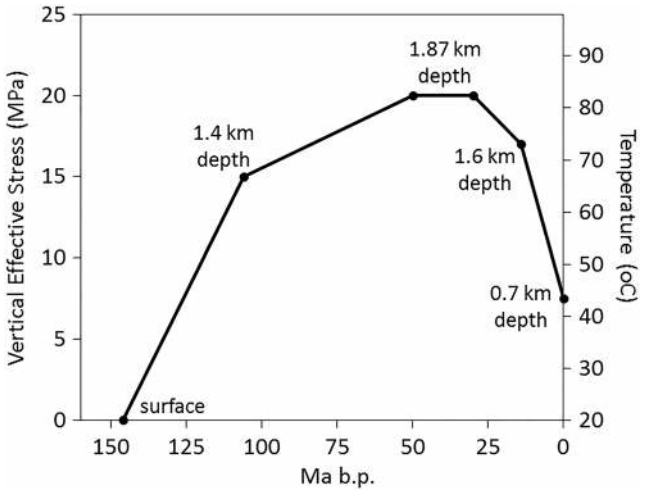

Figure 4. Burial history for Kimmeridge Bay Clay. Data derived from Nygård et al. (2004a, 2004b).

In addition to defining the shape of the yield surface, calibration of the model is carried out by simulating the mechanical compaction behavior for KWC using K_0 experimental data from (Nygård et al., 2004a). To this end, we have defined an axisymmetric single element model with boundary conditions representative of an oedometer test. A linearly increasing axial stress of up to 150 MPa followed by an unloading to 25 MPa has been imposed. The results after calibration are shown in Figure 3. During the experimental unloading path the axial stress decreased by up to 2 MPa; however, the simulation reaches softening conditions during the unloading when the stresses are decreased below ~25 MPa (not shown). Therefore, only the unloading path up to 25 MPa is considered. Note that the simulation is in good agreement with the experimental data. However, at a stress of 25 MPa, there is a mismatch of 0.04 units in void ratio between the experimental and modeled unloading paths. It should be noted that a better fit of the unloading path might be obtained using the original Cam Clay poroelasticity model (i.e., $A_{un} = 1$ in equation (7) as the void ratio would experience a higher increase during unloading. However, we consider that the chosen model is more appropriate for field simulations (e.g., we do not expect a large porosity increase during unloading, when a sample is collected from its original depth).

After calibration of the KWC mechanical properties we calibrated a diagenesis law to be representative of the transition from KWC to KBC. To this end we defined a single-element model that simulates the burial history of KBC for a small volume of sediment (the simulation tracks a material point during burial). The imposed stress and temperature conditions are shown in Figure 4. In order to calibrate the diagenetic processes from KWC/KBC transition we have assumed the following: (1) the change from KWC to KBC properties is a consequence of a single reaction (i.e., $N = 1$ in equation (9)) and (2) the reaction at the end of KBC burial history was completed (i.e., the diagenetic porosity loss at the end of the burial history equals the maximum diagenetic porosity loss. Note that we might obtain the same diagenetic porosity loss at the end of the burial history using a reaction defined with a higher maximum porosity loss if the time of exposure to temperatures above the threshold temperature is not enough to complete the reaction). In Figure 5 the simulation results are compared to KWC and KBC experimental compaction data. It can be seen that the simulated compaction path initially follows the KWC compaction curve until the sediment is compacted to a void ratio of 0.51 at a stress of ~15 MPa. Then, with ongoing burial the threshold temperature is reached and the chemical reaction starts to take place, resulting in a relatively large porosity loss until the sediment reaches its maximum burial depth (i.e., void ratio decreases from 0.51 to 0.24 for an effective stress increase of 5 MPa). Subsequently, there is an uplift and the unloading path follows the KBC overconsolidated compaction data until it reaches the current depth. We have subsequently simulated further unloading and reloading beyond the chemically enhanced yield stress at a temperature of 20 °C (mechanical compaction only) to test that the compaction path is representative of the KBC behavior (discontinuous line in Figure 5). It can be seen that the model agrees very well with the KBC data with a near to perfect match in the unloading path section.

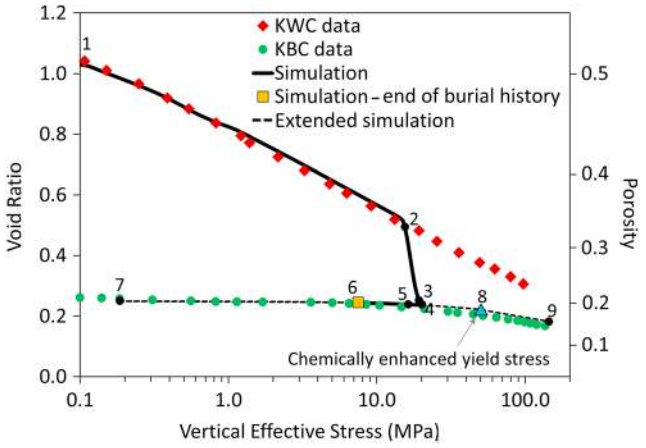

Figure 5. Simulated KBC history using a single-element model. The data have been obtained from Nygård et al. (2004a). The simulated compaction path corresponding to the KBC burial history stops at the point number 6, indicated with a yellow square, but the simulation is carried forward with further unloading and a subsequent reloading to high stresses beyond the yielding point (black discontinuous line). Points 1–6 correspond to stress states at the top surface, 1.4-km depth, 1.87-km depth, 1.87-km depth, 1.6-km depth, and 0.7-km depth, respectively, from the burial history in Figure 4. Point 7 is the minimum stress after unloading in the extended simulation; Point 8 is the chemically enhanced yield stress, and Point 9 is the maximum stress after reloading in the extended simulation. KBC = Kimmeridge Bay Clay; KWC = Kimmeridge Westbury Clay.

The stress path for the burial history of the Kimmeridge Clay is shown in Figure 6. During initial burial from the top surface to 1.4-km depth the stress state moves from points 1 to 2 following a K_0 path, during which the Kimmeridge Clay is compacted mechanically. With further burial from 1.4- to 1.87-km depth, the Kimmeridge Clay reaches the threshold temperature for the diagenetic processes to take place. The yield surface increases in size more rapidly than it would occur for a sediment compacting mechanically and so the stress path moves elastically inside the

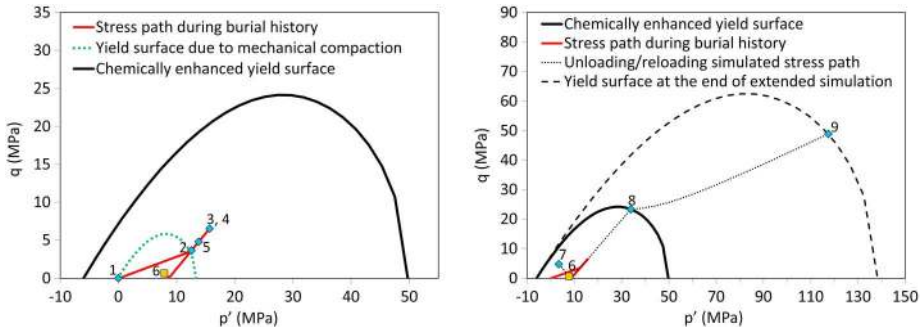

Figure 6. Stress path of the burial history of the Kimmeridge Clay. (a) Stress path until the end of burial history (present day). (b) Additional stress path during unloading and reloading at laboratory conditions (20 °C). The numbered points (from 1 to 9) on this figure correspond to those in Figure 5.

yield surface from the stress states indicated by points 2 to 3. Then from 50 to 30 Ma BP there is a hiatus period in which the sediment remains at 1.87-km depth and the yield surface increases slightly in size with negligible changes in stress (stress points 3 and 4). Subsequently, there is an uplift and erosion period from 30 to 14 Ma BP, which causes an uplift of the sediment to a depth of 1.6 km with the stress path unloading elastically from point 4 to point 5. From 14 Ma BP to present the sediment is uplifted to a depth of 0.7 km with the stress path going from point 5 to point 6. The latter represents the state in which the sample was retrieved. As previously described, we extended the simulation of the retrieved sample with further stress unloading and reloading at a constant temperature of 20 °C, with the aim of stopping any further diagenesis effects and to test the geomechanical behavior at laboratory conditions. With unloading, the stress path moves from point 6 to point 7, approaching the yield surface on the shear side. We stopped unloading at point 7 to prevent any softening and then reloaded the sample to a stress higher than 100 MPa. The stress path moves elastically from point 7 to point 6 and then to point 8, where the stress path met the yield surface on the cap side. At this point the stress state overcomes the diagenetic enhanced yield stress and the stress path causes plastic strains and hardening (yield surface size increase) moving from point 8 to point 9.

6. Effect of Nonmechanical Processes on Overpressure

Nonmechanical processes might have an effect on overpressure generation and evolution via two mechanisms: (1) the nonmechanical processes considered here decrease the pore volume (so either, the pore fluid flows out of the pore volume or pore pressure increases, or both) and (2) the reduction in porosity leads to a reduction in permeability, which will reduce the rate of overpressure dissipation generated by other mechanisms (e.g., increase in load by further sedimentation). In order to show the effects of nonmechanical processes on overpressure we simulate the UK Central Graben uniaxial strain scenario, previously presented by Gutierrez and Wangen (2005). The rationale of choosing this scenario is as follows: (1) their simulation accounted for a single lithology with KWC material properties, which facilitates our model build and (2)

Table 2
KWC to KBC Diagenesis Reaction Parameters

Parameter	Symbol	Value
Maximum diagenetic porosity loss	$(\Delta\phi)^{\mathrm{diag}}_{i\,\max}$	0.147
Porosity loss direction	—	Isotropic
Reaction constant	A	0.12 1/Ma
Temperature exponent	m_d	1.0
Initiation temperature	T_{ini}	70.0 °C
Porosity exponent	n_d	1.0
Maximum increase in tensile intercept	$(\Delta p_t)^{\mathrm{diag}}_{\max}$	6.0 MPa
Strength factor	F_{pc}	0.135
Maximum change in λ	$(\Delta\lambda)^{\mathrm{diag}}_{\max}$	−0.075
Maximum change in κ	$(\Delta\kappa)^{\mathrm{diag}}_{\max}$	−0.024

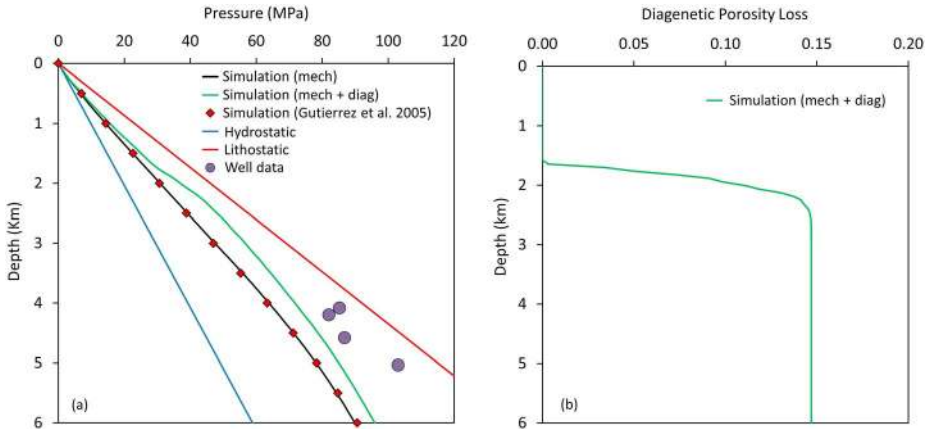

Figure 7. Results from the one-dimensional simulations of the UK Central Graben scenario described in Gutierrez and Wangen (2005). (a) Pore pressure. The two simulation curves correspond to cases with and without taking into account for diagenetic compaction processes and (b) diagenetic porosity loss.

they underpredicted overpressure relative to available well data and attributed that to the fact that they used a purely mechanical compaction model, whereas other nonmechanical processes might be involved in overpressure generation in that region. Thus, the scenario is a perfect benchmark to test if the incorporation of diagenesis can improve pore pressure predictions.

The model is defined to be one dimensional, consisting of an initial single KWC layer of 300-m height and accounting for 160 Ma of KWC deposition at a *gross* sedimentation rate (including the volume of voids at reference porosity) of 51.07 m/Ma (which is equivalent to the fully compacted sedimentation rate value of 25 m/Ma). For the KWC permeability-porosity law we use the KWC data for an undisturbed sample presented in Nygård et al. (2004a), which is the same as the following expression adopted by Gutierrez and Wangen (2005):

$$k = 4.8 \times 10^{-4} \exp\left[8.5(e - 1.06)\right] \tag{16}$$

where k is the permeability in mD and e is the void ratio.

We performed two simulations: a case accounting for mechanical compaction only and a case accounting for mechanical and nonmechanical compaction processes (with the diagenetic reaction data shown in Table 2. The results are presented in Figure 7. It can be observed that there is a good agreement between our mechanical compaction simulation and the one by Gutierrez and Wangen (2005) with no required calibration on permeability. It is evident that the incorporation of the diagenetic processes into the simulation lead to a pore pressure increase (Figure 7a). The simulation accounting for diagenetic processes predicts overpressures that are up to 9.2 MPa higher than the prediction by the mechanical compaction simulation at 2.6-km depth, where the diagenesis reaction is completed (Figure 7b). At greater depths the overpressure difference decreases as the generation of overpressure by diagenetic processes ceases. The difference in overpressure at 6-km depth is 6.0 MPa.

Despite the increase in overpressure predictions, the incorporation of diagenetic processes is not enough to explain the pore pressures observed in the region. The differences between the overpressure predicted

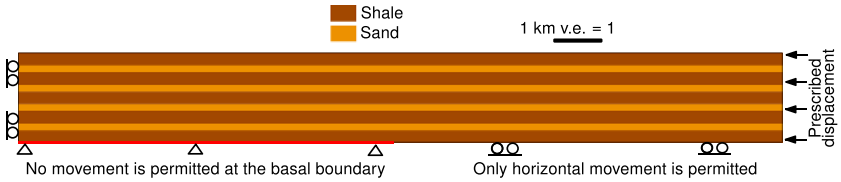

Figure 8. Thrust geometry after complete sedimentation and boundary conditions. The initial model geometry consisted of just the bottom-most shale layer. The initial thrust length is 30 km and the basal discontinuity is located at 14 km from the left-hand boundary.

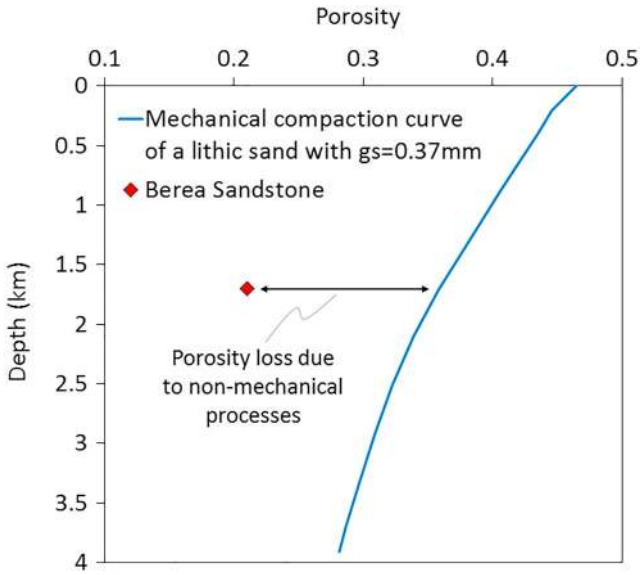

Figure 9. Experimental mechanical compaction curve of a lithic sand derived from Figure 4 in Chuhan et al. (2003) assuming a constant lithostatic gradient of 0.022 MPa/m and a constant hydrostatic gradient of 0.010 MPa/m compared to porosity data for a Berea Sandstone sample obtained from Wong et al. (1997) placed at its estimated maximum burial depth (neglecting elastic porosity recovery).

by the model that accounts for mechanical and nonmechanical compaction processes, and observed pore pressures, ranges from 7.0 to 17.6 MPa at 4.6 and 5.0 km, respectively, suggesting that additional overpressure generation processes need to be considered.

7. Effect of Nonmechanical Processes on Structural Style

As discussed previously, nonmechanical compaction processes result in a change in the geomechanical properties of sediments such as stiffness and strength. Thus, they might have an important impact on the structural deformation style resulting from tectonic activity; for example, the diagenetic overprint might result in an increased brittleness of the sediments, which might increase the likelihood of faulting. This hypothesis has been used previously by Roberts et al. (2015) to explain the formation of polygonal fault systems in passive settings. Thus, in the present section we define a model in order to show the effect of diagenesis on the predicted structural style in shortening environments. We will consider two cases: (1) a model that accounts for the mechanical compaction processes only and (2) a model that accounts for both the mechanical and nonmechanical compaction processes.

7.1. Model Definition

The model will consider three time stages: (1) a period of sedimentation, (2) a period of hiatus, and (3) a period of tectonic deformation. The simulations will be performed under hydrostatic conditions. The initial geometry consists of a 30-km-long and 0.6-km-high shale layer which is initialized under geostatic conditions with a ratio of the horizontal effective stress, $\sigma h'$, to the vertical effective stress, $\sigma v'$, equal to 0.8. The sedimentation stage captures the deposition of an alternating succession of five shale and four sand layers with initial thicknesses at depositional porosity of 0.3 and 0.6 km, respectively. The sedimentation rate is kept constant at 25 m/Ma. The complete sedimentation process ends after 156 Ma and the resulting geometry is shown in Figure 8. A hiatus of 50 Ma follows.

A discontinuity in the basal boundary conditions is prescribed at 14 km from the left boundary. The basal boundary to the left of the discontinuity is fully fixed in both horizontal and vertical directions. On the other hand, the basal boundary to the right of the discontinuity is fixed in the vertical direction whereas

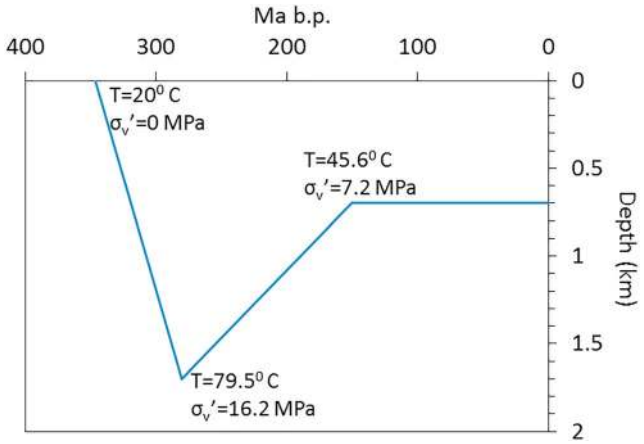

Figure 10. Burial history for Mississippian/Upper Devonian sediments in the Central Michigan Basin. The curve was obtained from Figure 7 in Charpentier (1987). Berea Sandstone is estimated to be of that age (e.g., see Figure 6 in Charpentier (1987). The temperature values result from assuming a surface temperature of 20 Â˚C and a temperature gradient of 35 Â˚C/km, and the vertical effective stress values result from the overlaying rock column with the calculated porosity values.

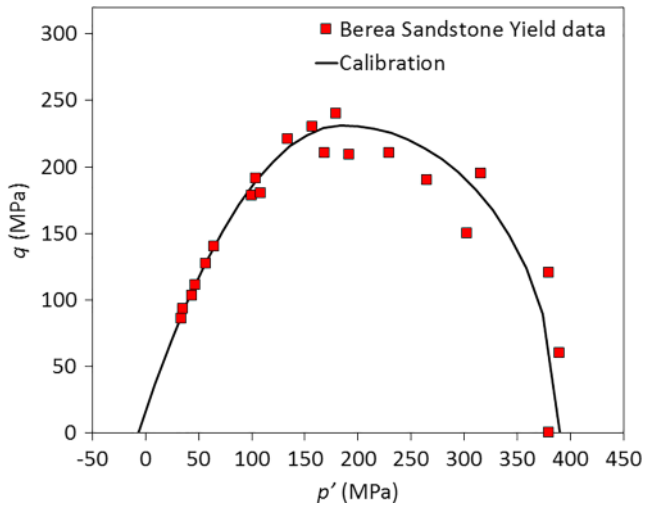

Figure 11. Berea Sandstone yield data from Wong et al. (1997) and calibrated yield surface shape.

free motion is allowed in the horizontal direction (the material has freedom to slide). Horizontal motion is prevented at the left-side boundary. The top surface will move freely as a consequence of the deformation. A prescribed displacement of 6 km on the right-side boundary will drive the compressive deformation during the 10 Ma of the tectonic stage. The temperature is 20 °C at the surface with a constant thermal gradient of 33 °C/km. The simulation is run under drained assumptions (i.e., pore pressures are kept hydrostatic).

The domain is discretized with an unstructured mesh of triangular elements with an average element size of 150 m. The mesh is adaptive, following an element size refinement law as a function of plastic strain that decreases the element length up to a value of 50 m for plastic strain values of 0.5 or more. This ensures enough resolution in active zones (in terms of strain) to capture fault initiation and propagation properly, whereas it keeps relatively coarse elements in inactive areas of the domain for the sake of the optimization of computational cost. The mechanical time step sizes have been defined so that each layer deposited is solved with 1×10^4 steps, the hiatus period is solved with 1×10^4 steps and the deformation period is solved with 2×10^5 steps.

The shale layers are modeled with the KWC/KBC material properties discussed in section 5 whereas the sand properties are discussed in the next section.

7.2. Sandstone Material Characterization

The material properties for sandstone layers have been calibrated using Berea Sandstone data as a benchmark. Berea Sandstone has a present-day porosity of 0.21 (Wong et al., 1997) with an estimated maximum burial depth of ~1.7 km (Charpentier, 1987). If these data are compared with the experimental mechanical compaction trend for a lithic sand with a similar grain size to that of Berea Sandstone (Chuhan et al., 2003), it becomes evident that processes other than pure mechanical compaction have played a role in the porosity loss of Berea Sandstone (see Figure 9). Therefore, the target has been to calibrate the sandstone mechanical compaction according to the experimental data from Chuhan et al. (2003) and then calibrate a single diagenesis reaction that will result in the sediment acquiring the Berea sandstone properties after simulation of Berea Sandstone burial history (Figure 10). The yield surface shape and target size are calibrated according to data from Wong et al. (1997; see Figure 11). The results after calibration are shown in Figure 12, and the constitutive model and diagenetic properties are shown in Tables 3 and 4, respectively.

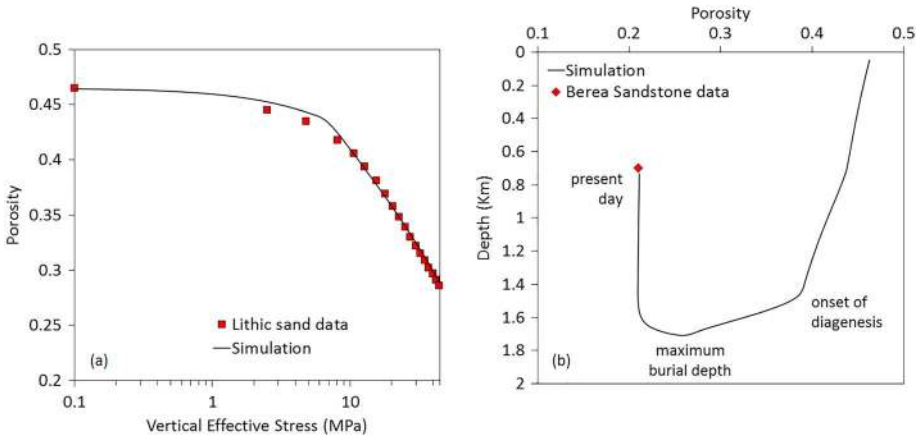

Figure 12. Results after calibration of Berea Sandstone properties. (a) Mechanical compaction calibration using experimental data from Chuhan et al. (2003). (b) Calibration of the diagenesis reaction by simulating the Berea Sandstone burial history shown in Figure 8 and targeting the Berea Sandstone sample porosity data from Wong et al. (1997).

Table 3
Calibrated Constitutive Model Properties for Berea Sandstone

Modeling feature	Parameter	Symbol	Value
Yield surface p'-q plane	Preconsolidation pressure at deposition	p_{c0}	6.9 MPa
	Tensile intercept at deposition	p_t	−0.3 MPa
	Friction parameter	β	67.5°
	Yield surface exponent	n	0.95
Yield surface shape in the deviatoric plane	Deviatoric plane exponent	N^{π}	0.25
	Deviatoric plane parameter	β_0^{π}	0.6
	Deviatoric plane parameter	β_1^{π}	0.6
Flow potential surface	Dilation parameter	ψ	62.5°
	Flow potential exponent	m	0.95
Hardening law and elasticity	Poisson ratio	μ	0.25
	Bulk modulus at deposition	K_{b0}	10 MPa
	Depositional porosity	ϕ_0	46.5%
	Hardening modulus	λ	0.18
	Slope of the unloading/reloading line	κ	0.08
	Porosity dependence factor	A_{un}	0.5
Grain properties	Grain density	ρ_s	2,650 kg/m^3
	Grain stiffness	k_s	20,000 MPa
Fluid properties	Fluid density	ρ_f	1,000 kg/m^3
	Fluid stiffness	k_f	2,000 MPa
	Fluid viscosity	μ_f	3.171×10^{-23} (MPa-Ma)

7.3. Results

The material grid for both cases is shown in Figure 13. It is evident that the diagenetic processes have had a significant effect on the predicted structural style. The case that accounts only for mechanical compaction has predicted a ductile structure, consisting of an anticlinal fold that developed above the basal boundary discontinuity (Figure 13a). The plastic strain contours show distributed strain with the maximum values concentrated near the basal discontinuity (Figure 14a). The shale layers show higher values of plastic strain than the more competent sand layers. On the other hand, the case that accounts for both mechanical and nonmechanical compaction has predicted a brittle structure consisting of a thrust fault that dips in the direction contrary to the shortening, with three conjugate back thrusts that were uplifted as the sediments were slipping above the thrust ramp. A small box-type-fold bounded by two kink bands is apparent to the right of

Table 4
Calibrated Diagenetic Reaction for Berea Sandstone

Parameter	Symbol	Value
Maximum diagenetic porosity loss	$(\Delta\phi)_{i\,\max}^{\text{diag}}$	0.179
Porosity loss direction	—	Isotropic
Reaction constant	A	0.24 1/Ma
Temperature exponent	m_d	1.0
Initiation temperature	T_{ini}	70.0 °C
Porosity exponent	n_d	1.0
Maximum increase in tensile intercept	$(\Delta p_t)_{\max}^{\text{diag}}$	6.7 MPa
Strength factor	F_{pc}	0.95
Maximum change in λ	$(\Delta\lambda)_{\max}^{\text{diag}}$	0.0
Maximum change in κ	$(\Delta\kappa)_{\max}^{\text{diag}}$	0.0

Note. We do not consider any change in λ and κ as data for the calibration of the constitutive model are not available.

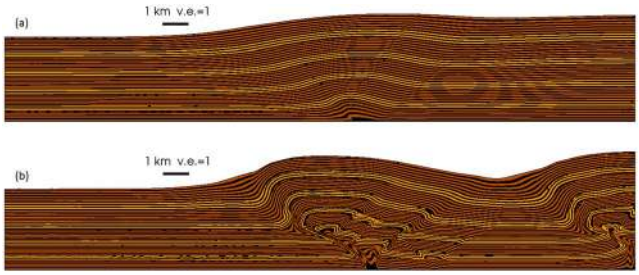

Figure 13. Model material grid after complete displacement. (a) Case considering mechanical compaction, (b) case considering mechanical and nonmechanical compaction. Brown layers consist of shale whereas yellow layers consist of sandstones.

the principal thrust. Brittle deformation is also evident near the moving boundary (Figure 13b). The plastic strain contours show strain localization on the fault planes (Figure 14b). Also it can be noted that the shale layers to the right of the thrust show lower values of plastic strain compared to the case that accounted for mechanical compaction only. This is because in the case with diagenesis, most of the shortening is accommodated by sliding over the thrust fault plane, whereas in the case that neglected diagenesis there is a greater amount of tectonic compaction. In Figure 15 the stress paths for a material point located within the oldest sandstone layer (see the final location the point in Figure 14) provide additional information on the reason behind the difference in the predicted structural style in both cases. In the case that accounts for mechanical compaction only (Figure 15a) there is an initial period of mechanical compaction because of the increased load due to burial (stress path from 1 to 2). At the end of burial the stress state lies on the yield surface. Then, the shortening stage starts and initially q decreases by 2.2 MPa with an increase in p' of 3 MPa because of an increase in the maximum horizontal ($\sigma H'$) and minimum horizontal ($\sigma h'$) effective stresses, whereas the vertical effective stress ($\sigma v'$) remains practically constant (stress path from 2 to 3). Subsequently, after the magnitude of $\sigma H'$ exceeds that of $\sigma v'$, there is an increase in both p' and q (stress path from 3 to 4). As the stress path moves from 2 to 3 and then from 3 to 4 there is mechanical compaction resulting from the tectonic load. In the case that accounts for both mechanical and nonmechanical compaction (Figure 15b), during burial there is an initial period of mechanical compaction followed by a period of nonmechanical compaction once the temperature exceeds the threshold temperature (stress path from 1 to 2). During nonmechanical compaction the yield surface increases considerably in size leaving the stress state inside the yield surface (stress state 2 and dotted yield surface). Due to this diagenetically induced overconsolidation, the stress state is situated on the shear side of the yield surface. Then, shortening starts, resulting in an increase in both p' and q. The stress path moves elastically until it meets the yield surface on the shear side (stress path from 2 to 3). Then, with ongoing shortening there is softening (decrease in the yield surface size and, therefore, decrease in strength) characterized by strain localization forming a plane of weakness, which is the continuum equivalent of a fault (stress path from 3 to 4). Therefore, the shortening is accommodated by displacement over the fault.

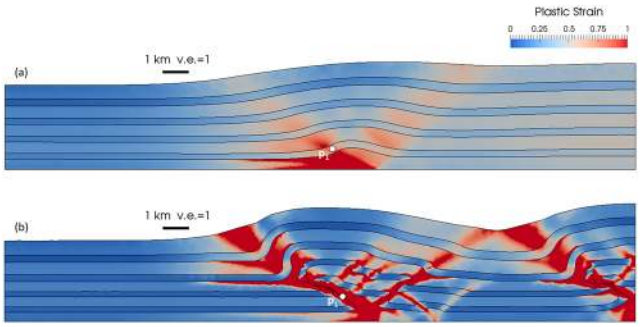

Figure 14. Plastic strain contours after complete displacement. (a) Case considering mechanical compaction, (b) case considering mechanical and nonmechanical compaction. P_1 indicates the position of a material point tracked within the oldest sandstone layer to plot the stress paths in Figure 14. Note that the initial position of P_1 was identical for both cases.

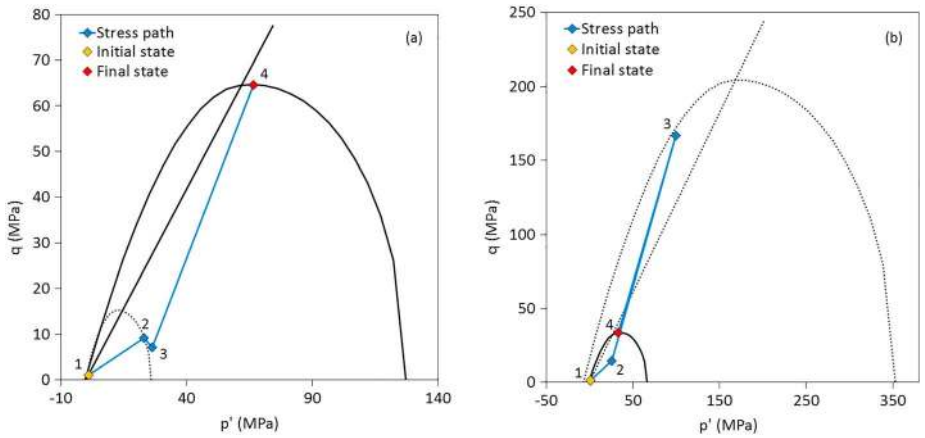

Figure 15. Stress paths for point P_1 shown in Figure 13. (a) Case considering mechanical compaction, (b) case considering mechanical and nonmechanical compaction. The numbers indicate the chronological order of the representative stress states that plot the stress path. The dotted black line corresponds to the yield surface before the onset of shortening, whereas the continuous black line corresponds to the final yield surface after shortening. The critical state line is also plotted for reference. Note that the case considering mechanical compaction is always in hardening conditions (stress path yielding to the right of the critical state line), and the final yield surface is greater than the yield surface before the onset of the shortening. On the other hand, the case accounting for mechanical and nonmechanical compaction shows softening behavior from stress state 3 to stress state 4 (stress path yielding to the left of the critical state line), and the final yield surface is smaller than the yield surface before the onset of shortening.

8. Discussion

We have presented a temperature-dependent diagenesis model that incorporates within geomechanical simulations: diagenetic porosity loss, diagenetic-induced change in geomechanical properties, and overpressure generation due to both the reduction in void volume and the consequent decrease in permeability. We have used experimental data for Kimmeridge Clay from Nygård et al. (2004a, 2004b, 2006) to calibrate a clay/shale model and data for Berea Sandstone (Wong et al., 1997) and a lithic sand (Chuhan et al., 2003) to calibrate a sand/sandstone model. The burial histories for Kimmeridge Clay (Nygård et al., 2004a) and Berea Sandstone (Charpentier, 1987) were used to estimate the temperature histories for both sediments and to calibrate the kinetics of the corresponding diagenetic reactions. The maximum temperatures for both sediments is estimated to be about 80 °C, assuming reasonable thermal gradients. Previous researchers have established 70 °C as the threshold temperature in conceptual chemical compaction models (Bjørlykke & Høeg, 1997; Bjørlykke, 1998; Dutta, 2002). Other researchers, however, suggested that at temperatures of about 65 °C smectite might already start to transform to illite in mudstones (Goulty et al., 2016) but that chemical compaction (porosity loss due to chemical reactions) does not start until temperatures of about 100 °C depending on the mineralogical composition and thermal histories of the sediments (Goulty et al., 2012). On the other hand, quartz cementation and chemical compaction in sandstones are often estimated to occur at temperatures above 80 °C (Bjørlykke et al., 2008; Walderhaug & Bjørkum, 2003) although it has recently been suggested that quartz cementation might start at 60 to 70 °C (Harwood et al., 2013). Regardless of the established temperature range for the occurrence of the individual chemical reactions, the data analyzed suggest that nonmechanical processes have contributed substantially to porosity loss and strength development in Kimmeridge Clay mudstone and Berea sandstone, both of which experienced a maximum estimated temperature of 80 °C. Therefore, we believe that our assumption of a threshold temperature of 70 °C for nonmechanical compaction is reasonable given the assumption of a single chemical reaction to lead the process. Reality, however, might be more complex and several reactions at different depths and temperature ranges might have contributed to the development of the sediments' present-day properties (e.g., shallow carbonate cementation). Furthermore, other rate-dependent processes such as deviatoric creep might also have played a role.

We have shown the effect of diagenesis on overpressure development by modeling the UK Central Graben scenario. We have validated the mechanical compaction model by direct comparison with Gutierrez and Wangen's (2005) results, obtaining a good agreement. Extending the model to incorporate the previously calibrated diagenesis model for Kimmeridge Clay resulted in an increase in overpressure of up to 9.2 MPa.

Despite the contribution of diagenesis to overpressure, the model is still insufficient to match the pressure data in the UK Central Graben. Several reasons could explain this. First, the model considers a single lithology, which might be an oversimplification of the true stratigraphy. For example, if there is a low-permeability shale layer at depths shallower than the pore pressure measurements, including this in the model would result in a further increase in pore pressure due to disequilibrium compaction. Second, we have considered that the change in permeability for a given diagenetic porosity loss is the same as the change that would produce an equivalent mechanical-induced porosity loss (we assume preservation of the porosity-permeability relationship). In reality, however, this might not be the case, as diagenetic processes might enhance grain orientation and involve textural changes in sediments that could change the porosity-permeability relationships (Bjørlykke, 1998; Goulty et al., 2012). Finally, other processes in addition to mechanical and nonmechanical compaction, which are not taken into account in our models, might have contributed to the overpressure observed in the UK Central Graben (e.g., fluid expansion mechanisms, buoyancy due to oil/gas column, gas generation, and lateral transfer).

Pore pressure prediction methods often rely on effective stress-porosity relationships (or porosity-dependent parameters such as sonic velocity or resistivity) and comparison of field observations with a normal compaction trend (NCT). If porosity at a given depth is higher than the NCT porosity, it is assumed that overpressure generated by disequilibrium compaction (pore fluid flow out of the pore spaces is slow compared to the loading rate) has helped to preserve porosity by decreasing the effective stress. Thus, knowing the effective stress that corresponds to such porosity, the depth and the hydrostatic and lithostatic pressures, overpressure can be estimated. While these assumptions may be valid for sediments at shallower depths above 2 km and temperatures below 65 °C, deeper and hotter sediments may not follow standard porosity-effective stress relationships due to both nonmechanical porosity reduction and overpressure generation by mechanisms other than disequilibrium compaction (Goulty, 1998; Hermanrud et al., 1998; Swarbrick et al., 2002). Some researchers have implemented alternative methods to predict overpressures in such scenarios by proposing either a diagenetic correction to the NCT (e.g., Lahann, 2002) or by attempting to capture pore pressure generation unloading mechanisms in their predictions (e.g., Bowers, 1995; Hart et al., 1995). The model presented in this paper can account for diagenetic porosity loss and overpressure generation and so is able to improve pore pressure predictions in diagenetic regimes.

Evidence for diagenetically induced overpressure is available in the literature. For example, Helset et al. (2002) concluded that up to 25% of the total overpressure in Halten Terrace and 80% in Gulf of Mexico might have been generated by chemical compaction, and Bolås et al. (2008) demonstrated that stress-insensitive chemical compaction needed to be invoked in basin models to obtain reasonable geological histories for the deeply buried North Sea Chalk sequences and match the low-porosity/high-overpressure data. Nguyen et al. (2016) showed that mechanical compaction alone cannot explain the high pore pressures measured at depths of about 3,000 m below seafloor in the Joetsu Basin and that the incorporation of chemical compaction in their models provides a plausible explanation for the measured magnitudes, and Goulty and Sargent (2016) showed that up to 20 MPa of overpressure are generated by unloading mechanisms (such as diagenesis) in Cretaceous mudstones in Haltenbanken. However, there is some debate concerning the mechanisms that lead to such overpressure generation. For example, whereas some researchers attribute the generation of overpressure to the volume changes involved in the smectite to illite transformation (e.g., Helset et al., 2002), others (e.g., Swarbrick et al., 2002) argued that such volume changes are too low to contribute significantly to overpressure generation and attribute the occurrence of overpressure to a load transfer from the grain framework to the pore fluid as the former is weakened during illitization, leading to pore collapse (Lahann, 2002; Lahann & Swarbrick, 2011; Swarbrick et al., 2002). The diagenesis model presented here allows the simulation of the macroscopic effects of diagenesis such as porosity loss and overpressure increase, regardless of the processes involved, if the model is adequately calibrated.

The data from Nygård et al. (2004a, 2004b) have shown that diagenesis increases the stiffness of the Kimmeridge Clay relative to an unaltered specimen mechanically compacted to the same porosity. Similar conclusions were obtained by Favero et al. (2016) in an experimental study on natural and remolded samples of Opalinus Clay. On the other hand, the diagenetically induced high porosity loss in Berea Sandstone resulted in a high preconsolidation pressure (Wong et al., 1997). Such chemically induced geomechanical changes have an important impact on the deformation behavior of sediments as they are expected to increase sediment brittleness (Bjørlykke & Høeg, 1997). This could explain the transition from ductile to brittle sediments as they are buried and exposed to relatively high temperatures (e.g., Roberts et al., 2015). We have

shown the impact that the calibrated diagenetic models have on the deformation style in a compressional setting. Whereas a purely mechanical model predicted a ductile structure, the model that accounted for the diagenetic effects has been able to predict faulting (brittle deformation). The key factor that changed the deformation style from ductile to brittle was the diagenesis-induced overconsolidation due to a more compacted structure. The yield surface increased in size with negligible changes in stress, causing the stress state to be located on the shear side of the yield surface before the onset of shortening. Thus, when compressive deformation started the stress path moved to meet the yield surface on the shear side resulting in strain localization and softening.

There are two ways to predict brittle deformation (without seeding the faults) with mechanical-only geomechanical models in compression: (1) Initialize the model with all or most of the sediments in place (zero or a minimum amount of deposition) and set the initial overconsolidation ratio to be high enough for the stress path to meet the yield surface on the shear side and (2) deposit the layers in a highly overconsolidated state, which would lead to unrealistic geological histories (i.e., too high initial strength and the omission of mechanical compaction with increasing burial). Thus, the diagenesis model presented here could be very beneficial in the geomechanical modeling of deposition and the evolution of sedimentary basins, helping to predict reasonable deformation structures relying on realistic sedimentation and burial histories. However, the data in the literature concerning the diagenetic effects on sediment geomechanical properties are scarce and more research is needed to help calibrate the models. For example we point out the following questions: How does diagenesis affect the yield surface shape? Does it have any effect on the residual friction? At what point might diagenesis increase the preconsolidation pressure in shales? What impact does diagenesis have on permeability? How can different diagenetic processes be adequately captured?

9. Conclusions

The first-order macroscopic effects of diagenetic processes on mudstone formations have been captured through a new phenomenological approach. To this end, the critical state-based SR4 constitutive model for mudstone rheology has been extended to include temperature-dependent, kinetic diagenesis processes within a hydromechanical framework. The main conclusions drawn on the ability of the model to reproduce laboratory experimental data and to predict overpressure and structural deformation are as follows:

- Previous research provides evidence concerning the effect of diagenesis on porosity loss and changes in sediment geomechanical properties (Nygård et al., 2004a, 2004b; Favero et al., 2016).
- We have presented a diagenesis model which accounts for nonmechanical compaction, diagenetically induced changes in sediment geomechanical properties, and diagenetically induced overpressure generation due to the loss in pore volume and the associated reduction in permeability.
- The calibrated model successfully captures experimental observations of Kimmeridge Clay.
- We have demonstrated the influence of diagenesis on overpressure in a UK Central Graben scenario. The incorporation of diagenesis leads to an increase in overpressure of 9.2 MPa. A greater effect is expected in basins with higher sedimentation rates due to the diagenetically triggered reduction of permeability and therefore higher degree of disequilibrium compaction.
- We have demonstrated the control of diagenesis on the predicted structural style using geomechanical models. Models that neglected the diagenetic effects predicted ductile structures, whereas the incorporation of diagenesis led to the prediction of a thrust fault and brittle deformation.

Acknowledgments
This work was undertaken within the GeoPOP (Geosciences Project on OverPressure) project, which is sponsored by BG Group, BP, Chevron, ConocoPhillips, DONG Energy, E.ON Ruhrgas, ENI, Petrobras, Petronas, Statoil, Total, and Tullow Oil. We thank the anonymous reviewers and the Associate Editor, Brandon Dugan, whose suggestions and comments helped to improve the paper. The data used are listed in the references and tables and the output of simulations are available online (https://doi.org/10.6084/m9.figshare.7837625.v1).

References

Ajdukiewicz, J. M., & Lander, R. H. (2010). Sandstone reservoir quality prediction: The state of the art. *AAPG Bulletin*, *94*, 1083–1091.

Albertz, M., & Lingrey, S. (2012). Critical state finite element models of contractional fault-related folding: Part 1. Structural analysis. *Tectonophysics*, *576-577*, 133–149.

Albertz, M., & Sanz, P. F. (2012). Critical state finite element models of contractional fault-related folding: Part 2. Mechanical analysis. *Tectonophysics*, *576-577*, 150–170.

Allwardt, J. R., Michael, G. E., Shearer, C. R., Heppard, P. D., & Ge. H. (2009). 2D modeling of overpressure in a salt withdrawal basin, Gulf of Mexico, USA. *Marine and Petroleum Geology*, *26*, 464–473.

Aplin, A. C., Matenaar, I. F., McCarty, D. K., & van der Pluijm, B. A. (2006). Influence of mechanical compaction and clay mineral diagenesis on the microfabric and pore-scale properties of deep water Gulf of Mexico mudstones. *Clays and Clay Minerals*, *54*, 501–515.

Audet, D. M. (1995). Mathematical modelling of gravitational compaction and clay dehydration in thick sediment layers. *Geophysical Journal International*, *122*, 283–298.

Bekele, E. B., Johnson, M. D., & Higgs, W. G. (2001). Numerical modelling of overpressure generation in the barrow sub-basin, northwest Australia. *APPEA Journal*, *41*, 595–608.

Berger, G., Velde, B., & Aigouy, T. (1999). Potassium sources and illitization in Texas Gulf coast shale diagenesis. *Journal of Sedimentary Research*, *69*, 151–157.

Bjørlykke, K. (1998). Clay mineral diagenesis in sedimentary basins—A key to the prediction of rock properties. Examples from the North Sea basin. *Clay Minerals*, *33*(1), 15–34.

Bjørlykke, K., & Høeg, K. (1997). Effects of burial diagenesis on stress, compaction and fluid flow in sedimentary basins. *Marine and Petroleum Geology*, *14*, 267–276.

Bjørlykke, K., Jahren, J., Mondol, N. H., Marcussen, O., Croize, D., Peltonen, C., & Thyberg, B. (2008). Sediment compaction and rock properties. In *AAPG International Conference and Exhibition* (pp. 1–8). Cape Town, South Africa.

Bolås, H. M. N., Hermanrud, C., Schutter, T. A., & Teige, G. M. G. (2008). Is stress-insensitive chemical compaction responsible for high overpressures in deeply buried North Sea chalks? *Marine and Petroleum Geology*, *25*, 565–587.

Bolås, H. M. N., Hermanrud, C., & Teige, G. M. G. (2004). Origin of overpressures in shales: Constraints from basin modeling. *AAPG Bulletin*, *88*, 193–211.

Bowers, G. L. (1995). Pore pressure estimation from velocity data: Accounting for overpressure mechanisms besides undercompaction. *SPE Drilling and Completion*, *10*(2), 89–95.

Broichhausen, H., Littke, R., & Hantschel, T. (2005). Mudstone compaction and its influence on overpressure generation, elucidated by a 3D case study in the North Sea. *International Journal of Earth Sciences*, *94*(5), 956–978.

Chadwick, R. A. (1985). Permian, Mesozoic and Cenozoic structural evolution of England and Wales in relation to the principles of extension and inversion tectonics. In A. Whittaker (Ed.), *Atlas of onshore sedimentary basins in England and Wales: Post-Carboniferous tectonics and stratigraphy* (pp. 9–25). Glasgow: Blackie.

Charpentier, R. R. (1987). A summary of petroleum plays and characteristics of the Michigan basin. Reston, VA: US Geological Survey.

Chuhan, F. A., Kjeldstad, A., Bjørlykke, K., & Høeg, K. (2003). Experimental compression of loose sands; relevance to porosity reduction during burial in sedimentary basins. *Canadian Geotechnical Journal*, *40*, 995–1011.

Colton-Bradley, V. A. C. (1987). Role of pressure in smectite dehydration-effects on geopressure and smectite to illite transition. *AAPG Bulletin*, *71*, 1414–1427.

Crook, A. J. L. (2013). *ParaGeo: A finite element model for coupled simulation of the evolution of geological structures*. Swansea, UK: Three Cliffs Geomechanical Analysis.

Day-Stirrat, R. J., Loucks, R. G., Milliken, K. L., Hillierc, S., & van der Pluijm, B. A. (2008). Phyllosilicate orientation demonstrates early timing of compactional stabilization in calcite-cemented concretions in the Barnett shale (late mississippian), Fort Worth basin, Texas (USA). *Sedimentary Geology*, *208*(1–2), 27–35.

Day-Stirrat, R. J., Milliken, K. L., Dutton, S. P., Loucks, R. G., Hillier, S., Aplin, A. C., & Schleicher, A. M. (2010). Open-system chemical behavior in deep Wilcox group mudstones, Texas Gulf coast, USA. *Marine and Petroleum Geology*, *27*, 1804–1818.

Dutta, D. C. (2002). Deepwater geohazard prediction using prestack inversion of large offset *P*-wave data and rock model. *The Leading Edge*, *21*, 193–198.

Eberl, D., & Hower, J. (1976). Kinetics of illite formation. *Geological Society of America Bulletin*, *87*, 1326–1330.

Elliott, W. C., & Matisoff, G. (1996). Evaluation of kinetic models for the smectite to illite transformation. *Clays and Clay Minerals*, *44*, 77–87.

Favero, V., Ferrari, A., & Laloui, L. (2016). On the hydro-mechanical behaviour of remoulded and natural Opalinus clay shale. *Engineering Geology*, *208*, 128–135.

Flemings, P. B., & Lupa, J. A. (2004). Pressure prediction in the Bullwinkle basin through petrophysics and flow modeling (Green Canyon 65, Gulf of Mexico). *Marine and Petroleum Geology*, *21*(10), 1311–1322.

Freed, R. L., & Peacor, D. R. (1989). Variability in temperature of the smectite illite reaction in Gulf Coast sediments. *Clay Minerals*, *24*, 171–180.

Gao, B., Flemings, P., Nikolinakou, M., Saffer, D., & Heidari, M. (2018). Mechanics of fold-and-thrust belts based on geomechanical modeling. *Journal of Geophysical Research: Solid Earth*, *123*, 4454–4474. https://doi.org/10.1029/2018JB015434

Goulty, N. R. (1998). Relationship between porosity and effective stress in shales. *First Break*, *16*, 413–419.

Goulty, N. R., Ramdhan, A. M., & Jones, S. J. (2012). Chemical compaction of mudrocks in the presence of overpressure. *Petroleum Geoscience*, *18*, 471–479.

Goulty, N. R., & Sargent, C. (2016). Compaction of diagenetically altered mudstones—part 2: Implications for pore pressure estimation. *Marine and Petroleum Geology*, *77*, 806–818.

Goulty, N. R., Sargent, C., Andras, P., & Aplin, A. C. (2016). Compaction of diagenetically altered mudstones—part 1: Mechanical and chemical contributions. *Marine and Petroleum Geology*, *77*, 703–713.

Gutierrez, M., & Wangen, M. (2005). Modeling of compaction and overpressuring in sedimentary basins. *Marine and Petroleum Geology*, *22*, 351–363.

Hamilton, E. L. (1959). Thickness and consolidation of deep sea sediments. *Bulletin of the Geological Society of America*, *70*, 1399–1424.

Hart, B. S., Flemings, P. B., & Desphande, A. (1995). Porosity and pressure; role of compaction disequilibrium in the development of geopressures in a Gulf Coast Pleistocene basin. *Geology*, *23*, 45–48.

Harwood, J., Aplin, A. C., Fialips, C. I., Iliffe, J. E., Kozdon, R., Ushikubo, T., & Valley, J. W. (2013). Quartz cementation history of sandstones revealed by high-resolution SIMS oxygen isotope analysis. *Journal of Sedimentary Research*, *83*, 522–530.

Helset, H. M., Lander, R. H., Matthews, J. C., Reemst, P., Bonnell, L. M., & Frette, I. (2002). The role of diagenesis in the formation of fluid overpressures in clastic rocks. In A. G. Koestler & R. Hundsdale (Eds.), *Hydrocarbon seal quantification* (Vol. 11, pp. 37–50). Stavanger, Norway: Elsevier Science.

Hermanrud, C., Wensaas, L., Teige, G. M. G., Nordgård Bolås, H. M., & Hansen, S. (1998). Shale porosities from well logs on Haltenbanken (offshore Mid-Norway) show no influence of overpressuring. In B. E. Law, G. F. Ulmishek, & V. I. Slavin (Eds.), *Abnormal pressures in hydrocarbon environments* (Vol. 70, pp. 65–87). Tulsa: AAPG, Memoir.

Hill, P. R. (1987). Chalk solution structures in cores from deep sea drilling project Leg 94, Norfolk Virginia to St. Johns Newfoundland. In W. F. Ruddiman, & R. B. Kidd (Eds.), *Initial reports of the deep sea drilling project leg* (Vol. 94, pp. 1129–1143). Washington, D. C: Printing Office.

Ho, N.-C., Peacor, D. R., & van der Pluijm, B. A. (1999). Preferred orientation of phyllosilicates in Gulf Coast mudstones and relation to the smectite-illite transition. *Clays and Clay Minerals*, *47*, 495–504.

Hower, J., Eslinger, E. V., Hower, M. E., & Perry, E. A. (1976). Mechanism of burial metamorphism of argillaceous sediment: 1. Mineralogical and chemical evidence. *Geological Society of America Bulletin*, *87*(5), 725–737.

Isaacs, C. M. (1981). Porosity reduction during diagenesis of the Monterey Formation, Santa Barbara coastal area, California. In R. E. Garrison, & R. G. Douglas (Eds.), *The Monterey Formation and related siliceous rocks of California* (pp. 257–271). Los Angeles: SEPM Pacific Section.

Ishii, E., Sanada, H., Iwatsuki, T., Sugita, Y., & Kurikami, H. (2011). Mechanical strength of the transition zone at the boundary between opal-A and opal-CT zones in siliceous rocks. *Engineering Geology*, *122*, 214–221.

Kamp, P. C. (2008). Van de smectite illite muscovite transformations, quartz dissolution, and silica release in shales. *Clays and Clay Minerals*, *56*(1), 66–81.

Katahara, K. W. (2006). Overpressure and shale properties: Stress unloading or smectite-illite transformation? *Society of Exploration Geophysicists Annual Meeting* (pp. 1520–1524). Louisiana, USA: New Orleans.

Keller, M. A., & Isaacs, C. M. (1985). An evaluation of temperature scales for silica diagenesis in diatomaceous sequences including a new approach based on the miocene Monterey Formation, California. *Geo-Marine Letters*, *5*, 31–35. https://doi.org/10.1007/BF02629794

Kjeldstad, A., Skogseid, J., Langtangen, H. P., Bjørlykke, K., & Høeg, K. (2003). Differential loading by prograding sedimentary wedges on continental margins: An arch-forming mechanism. *Journal of Geophysical Research*, *108*(B1), 2036. https://doi.org/10.1029/2001JB001145

Kvilhaug, T. (1995). *Rock mechanical properties of mudrocks in relation to petrology*. Trondheim, Norway, Norwegian University of Science and Technology.

Lahann, R. W. (2002). Impact of smectite diagenesis on compaction modeling and compaction equilibrium. In A. R. Huffman, & G. L. Bowers (Eds.), *Pressure regimes in sedimentary basins and their prediction* (pp. 61–72). Houston, TX: AAPG Memoir.

Lahann, R. W., & Swarbrick, R. (2011). Overpressure generation by load transfer following shale framework weakening due to smectite diagenesis. *Geofluids*, *11*, 362–375.

Mallon, A. J., & Swarbrick, R. E. (2002). A compaction trend for non-reservoir North Sea chalk. *Marine and Petroleum Geology*, *19*, 527–539.

McBride, E. F. (1989). Quartz cement in sandstones: A review. *Earth-Science Reviews*, *26*, 69–112.

Meadows, D., & Davies, R. J. (2009). Predicting porosity reduction due to silica diagenesis using seismic reflection data. *Marine and Petroleum Geology*, *26*(8), 1543–1553.

Muir Wood, D. (1990). *Soil behaviour and critical state soil mechanics*. Cambridge: Cambridge University Press.

Neumaier, M., Littke, R., Hantschel, T., Maerten, L., Joonnekindt, J.-P., & Kukla, P. (2014). Integrated charge and seal assessment in the Monagas fold and thrust belt of Venezuela. *AAPG Bulletin*, *98*(7), 1325–1350.

Nguyen, B. T., Kido, M., Okawa, N., Fu, H., Kakizaki, S., & Imahori, S. (2016). Compaction of smectite-rich mudstone and its influence on pore pressure in the deepwater Joetsu basin, Sea of Japan. *Marine and Petroleum Geology*, *78*, 848–869.

Nikolinakou, M. A., Flemings, P. B., & Hudec, M. R. (2014). Modeling stress evolution around a rising salt diapir. *Marine and Petroleum Geology*, *51*, 230–238.

Nygård, R., Gutierrez, M., Bratli, R. K., & Høeg, K. (2006). Brittle-ductile transition, shear failure and leakage in shales and mudrocks. *Marine and Petroleum Geology*, *23*(2), 201–212.

Nygård, R., Gutierrez, M., Gautam, R., & Høeg, K. (2004a). Compaction behaviour of argillaceous sediments as function of diagenesis. *Marine and Petroleum Geology*, *21*(3), 349–362.

Nygård, R., Gutierrez, M., Høeg, K., & Bjørlykke, K. (2004b). Influence of burial history on microstructure and compaction behaviour of Kimmeridge clay. *Petroleum Geoscience*, *10*(3), 259–270.

Obradors-Prats, J., Rouainia, M., Aplin, A. C., & Crook, A. J. L. (2016). Stress and pore pressure histories in complex tectonic settings predicted with coupled geomechanical-fluid flow models. *Marine and Petroleum Geology*, *76*, 464–477.

Obradors-Prats, J., Rouainia, M., Aplin, A. C., & Crook, A. J. L. (2017a). Assessing the implications of tectonic compaction on pore pressure using a coupled geomechanical approach. *Marine and Petroleum Geology*, *79*, 31–43.

Obradors-Prats, J., Rouainia, M., Aplin, A. C., & Crook, A. J. L. (2017b). Hydromechanical modeling of stress, pore pressure, and porosity evolution in fold-and-thrust belt systems. *Journal of Geophysical Research: Solid Earth*, *122*, 9383–9403. https://doi.org/10.1002/2017JB014074

Osborne, M. J., & Swarbrick, R. E. (1997). Mechanisms for generating overpressure in sedimentary basins: A reevaluation. *AAPG Bulletin*, *81*, 1023–1041.

Osborne, M. J., & Swarbrick, R. E. (1999). Diagenesis in North Sea HPHT clastic reservoirs—Consequences for porosity and overpressure prediction. *Marine and Petroleum Geology*, *16*, 337–353.

Oye, O. J., Aplin, A. C., Jones, S. J., Gluyas, J. G., Bowen, L., Orland, I. J., & Valley, J. W. (2018). Vertical effective stress as a control on quartz cementation in sandstones. *Marine and Petroleum Geology*, *98*, 640–652.

Peltonen, C., Marcussen, Ø, Bjørlykke, K., & Jahren, J. (2009). Clay mineral diagenesis and quartz cementation in mudstones: The effects of smectite to illite reaction on rock properties. *Marine and Petroleum Geology*, *26*, 887–898.

Penn, I. E., Chadwick, R. A., Holloway, S., Roberts, G., Paraoh, T. C., Allsop, J. M., et al. (1987). Principal features of the hydrocarbon prospectivity of the Wessex-Channel Basin, UK. In J. Brooks, & K. Glennie (Eds.), *Petroleum Geology of North West Europe* (pp. 109–118). London: Graham and Trotman.

Roberts, D. T., Crook, A. J. L., Profit, M. L., & Cartwright, J. A. (2015). Investigating the evolution of polygonal fault systems using geomechanical forward modeling. In *49th US Rock Mechanics/Geomechanics Symposium*, ARMA, San Francisco, CA, USA, pp. 13.

Rouainia, M., & Muir Wood, D. (2006). Computational aspects in finite strain plasticity analysis of geotechnical materials. *Mechanics Research Communications*, *33*(2), 123–133.

Sample, J. C. (1990). The effect of carbonate cementation of underthrust sediments on deformation styles during underplating. *Journal of Geophysical Research*, *95*(B6), 9111–9121.

Schneider, F., & Hay, S. (2001). Compaction model for quartzose sandstones application to the Garn Formation, Haltenbanken, mid-Norwegian continental shelf. *Marine and Petroleum Geology*, *18*, 833–848.

Schneider, F., Potdevin, J. L., Wolf, S., & Faille, I. (1996). Mechanical and chemical compaction model for sedimentary basin simulators. *Tectonophysics*, *263*, 307–317.

Schneider, F., Wolf, S., Faille, I., & Pot, D. (2000). A 3D basin model for hydrocarbon potential evaluation: Application to congo offshore. *Oil & Gas Science and Technology - Revue de l'IFP*, *55*(1), 3–13.

Scholle, P. A. (1977). Chalk diagenesis and its relation to petroleum exploration: Oil from chalks, a modern miracle? *AAPG Bulletin*, *61*, 982–1009.

Selley, R. C., & Stoneley, R. (1987). Petroleum habitat in South Dorset. In J. Brooks, & K. W. Glennie (Eds.), *Petroleum geology of north west Europe* (pp. 139–148). London: Graham & Trotman.

Smart, K. J., Ferrill, D. A., Morris, A. P., & McGinnis, R. N. (2012). Geomechanical modeling of stress and strain evolution during contractional fault-related folding. *Tectonophysics*, *576-577*, 171–196.

Spinelli, G. A., Mozley, P. S., Tobin, H. J., Hoffman, M. B., & Bellew, G. M. (2007). Underwood diagenesis, sediment strength, and pore collapse in sediment approaching the Nankai trough subduction zone. *Geological Society of America Bulletin*, *119*(3/4), 377–390.

Stoneley, R. (1982). The structural development of the Wessex basin. *Journal of the Geological Society of London*, *139*, 543–554.

Swarbrick, R. E., Osborne, M. J., & Yardley, G. S. (2002). Comparison of overpressure magnitude resulting from the main generating mechanisms. In A. R. Huffman, & G. L. Bowers (Eds.), *Pressure regimes in sedimentary basins and their prediction* (pp. 1–12). Houston, TX: AAPG Memoir.

Tada, R. (1991). Compaction and cementation in siliceous rocks and their possible effect on bedding enhancement. In G. Einsele, W. Ricken, & A. Seilacher (Eds.), *Cycles and events in stratigraphy* (pp. 480–491). Berlin, Germany: Springer.

Tada, R., & Siever, R. (1989). Pressure solution during diagenesis. *Annual Review of Earth and Planetary Sciences*, *17*, 89–118.

Taylor, T. R., Giles, M. R., Hathon, L. A., Diggs, T. N., Braunsdorf, N. R., Birbiglia, G. V., et al. (2010). Sandstone diagenesis and reservoir quality prediction: Models, myths, and reality. *AAPG Bulletin*, *94*, 1093–1132.

Terzaghi, K. (1923). Die berechnung der durchlässigkeitsziffer des tones aus dem verlauf der hydrodynamischen spannungserscheinungen. *Sitzungber. Akad. Wiss. Wien*, *132*, 125–138.

Thornton, D. A., & Crook, A. J. L. (2014). Predictive modelling of the evolution of fault structure: 3-D modelling and coupled geomechanical/flow simulation. *Rock Mechanics and Rock Engineering*, *47*(5), 1533–1549.

Thyberg, B., & Jahren, J. (2011). Quartz cementation in mudstones: Sheet-like quartz cement from clay mineral reactions during burial. *Petroleum Geoscience*, *17*, 53–63.

Underhill, J. R., & Stoneley, R. (1998). Introduction to the development, evolution and petroleum geology of the Wessex basin. *Geological Society, Special Publications*, *133*, 1–18.

Velde, B., & Vasseur, G. (1992). Estimation of the diagenetic smectite to illite transformation in time-temperature space. *American Mineralogist*, *77*, 967–976.

Walderhaug, O. (1994). Temperatures of quartz cementation in jurassic sandstones from the Norwegian continental shelf—Evidence from fluid inclusions. *Journal of Sedimentary Research*, *64*, 311–323.

Walderhaug, O. (1996). Kinetic modeling of quartz cementation and porosity loss in deeply buried sandstone reservoirs. *AAPG Bulletin*, *80*(5), 731–745.

Walderhaug, O., & Bjørkum, P. A. (2003). The effect of stylolite spacing on quartz cementation in the lower Jurassic Sto formation, southern Barents Sea. *Journal of Sedimentary Research*, *73*(2), 146–156.

Wong, T.-F., Christian, D., & Wenlu, Z. (1997). The transition from brittle faulting to cataclastic flow in porous sandstones: Mechanical deformation. *Journal of Geophysical Research*, *102*(B2), 3009–3025.

Worden, R., & Morad, S. (2000). Quartz cementation in oil field sandstones: A review of the key controversies, *Quartz cementation in sandstones* (Vol. 29, pp. 1–20). Malden, MA: Blackwell Science.